Journal of ELECTRONIC MATERIALS, Vol. 49, No. 7, 2020
https://doi.org/10.1007/s11664-020-08144-4

Role of Morphology of Surfactant-Free Nanoparticles in Organic Photovoltaics

DARMAWATI DARWIS,[1,4] ELISA SESA,[1] SYAHRUL ULUM,[1] NATALIE P. HOLMES,[2] KRISHNA FERON,[2] MAHIR THAMEEL,[2,3] RIKU CHOWDHURY,[2] DEDY FARHAMSAH,[1] LEVI TEGG,[2] XIAOJING ZHOU,[2] PAUL C. DASTOOR,[2] and WARWICK J. BELCHER[2]

1.—Centre for Organic Electronics, University of Tadulako, Palu, Indonesia. 2.—Centre for Organic Electronics, University of Newcastle, Callaghan, NSW 2308, Australia. 3.—Department of Physics, College of Education for Pure Science, University of Anbar, Ramadi 31001, Iraq. 4.—e-mail: Darmawati.Darwis@uon.edu.au

Nanoparticulate (NP) films and organic photovoltaic devices have been fabricated from poly(3-hexylthiophene):phenyl C_{61} butyric acid methyl ester (P3HT:$PC_{61}BM$) NP aqueous dispersions prepared by the precipitation method. The NP inks were stable for more than 4 days, and nanoparticle organic photovoltaic (NP-OPV) devices with efficiency (η) of 1% were fabricated. Detailed analysis of the morphology and performance of the precipitated NP-OPV devices indicated that an optimal blend is responsible for the photocurrent and efficiency observed. These results were confirmed by grazing-incidence x-ray diffraction (GIXRD) analysis, which revealed that the precipitated NPs were resistant to thermal phase segregation, allowing thermal conditioning of the NP films. These results show that precipitated NPs provide a pathway to thermally stable NP-OPV devices with higher photocurrents and efficiencies, approaching those of optimal bulk heterojunction (BHJ) OPV devices.

Key words: Organic photovoltaic cells (OPV), nanoparticle (NP), nanoparticle morphology, precipitation, surfactant-free, ink stability

INTRODUCTION

Organic photovoltaic (OPV) devices have attracted interest in recent times due to their use of nontoxic active materials and the ability to print them at scale.[1] However, large-scale production has been hindered by the need for halogenated and aromatic organic solvents in the printing process.[2] Whilst progress is being made towards OPV fabrication using more benign organic solvents,[2] the low solubility of currently available active materials in these solvents severely limits their utilization. Consequently, there is growing interest in the development of nanoparticulate OPV devices which can be printed from aqueous or benign organic suspensions.[3–9] Typically, these suspensions are prepared by a miniemulsion process and a surfactant is required to stabilize the resultant ink, with shelf lifetimes on the order of months having been demonstrated.

In general, devices fabricated from nanoparticulate (NP) inks exhibit lower efficiencies than those prepared using conventional organic solvents.[10] This lower performance has been attributed to the effect of residual surfactant trapped in the active layer, which may act as a source of charge trapping.[11] Additionally, nonoptimal phase separation occurs within the nanoparticles during the synthesis, with a core–shell structure being observed, which is believed to hinder charge generation and especially transport in these materials.[10,12–14]

(Received November 6, 2019; accepted April 2, 2020; published online April 10, 2020)

To alleviate the need for surfactant, a precipitation method for the formation of nanoparticle suspensions has been developed, wherein an organic solution of the active material blend is deposited into a suitable nonsolvent (typically a green solvent such as an alcohol).[15] This method has the added advantage of producing nanoparticles with a more blended morphology of the donor and acceptor components.[15,16] Devices prepared from the resultant inks show efficiencies comparable to or better than their surfactant-stabilized analogs, but the inks themselves are less stable and must be used immediately for device fabrication to avoid aggregation and dissolution. Furthermore, due to this inherent instability, precipitated inks necessarily have considerably lower mass loadings of active materials. As a result, multiple deposition steps are required to achieve an active layer which is devoid of pinholes and thick enough for consistent device performance.[17,18] However, the evolution of the film morphology and device performance as functions of multiple layer deposition is not well understood, and the mechanism by which the precipitated NPs can outperform their surfactant-containing counterparts is not clear.

We show herein that precipitated nanoparticle inks which are stable for several days can be synthesized by optimizing the active material loadings. The performance and active layer morphology of these inks were assessed as a function of sequential layer deposition and compared with equivalent surfactant-stabilized inks using a range of techniques including grazing-incidence x-ray diffraction (GIXRD) analysis, atomic force microscopy (AFM), transmission electron microscopy (TEM), scanning electron microscopy (SEM), ultraviolet–visible (UV–Vis) spectroscopy, photoluminescence (PL) spectroscopy, and OPV device characterization methods including current density–voltage (J–V) and external quantum efficiency (EQE) plots. The significant advantages of the highly blended precipitated NP morphology are explored and discussed.

EXPERIMENTAL PROCEDURES

Poly(3-hexylthiophene) (P3HT) was obtained from the Centre for Organic Electronics (COE), and phenyl C_{61} butyric acid methyl ester ($PC_{61}BM$) was purchased from Lumtec Co. Chloroform and anhydrous ethanol were obtained from Sigma Aldrich. All chemicals were used as received.

Nanoparticle Suspension Synthesis

Surfactant-free semiconducting polymeric nanoparticles were prepared according to the precipitation method previously used for P3HT:$PC_{61}BM$ nanoparticle formation.[15] P3HT (5 mg) and $PC_{61}BM$ were dissolved in chloroform (0.5 wt%) and stirred for 60 min with gentle heating. The chloroform ($CHCl_3$) solution was loaded into a syringe and added dropwise to a stirred solution of absolute ethanol (4 mL). A key difference from previous work reported by Darwis et al.[15] is that, once a nanoparticle suspension was obtained, it was immediately heated on a hotplate at 60°C for 3.5 h to remove $CHCl_3$. A nanoparticle suspension that was stable for more than 4 days was thus obtained.

Nanoparticle Suspension and Film Characterization

Dynamic light scattering (DLS, Zetasizer Nano-ZS; Malvern Instruments, UK) was used to measure the distribution of particle sizes in the aqueous dispersions. SEM was performed using an ultra-high-resolution field-emission-gun scanning electron microscope (Zeiss Sigma VP). Samples were measured at an accelerating voltage of 2 kV in the magnification range from 5000× to 150,000×. All SEM samples were spin-coated (3000 rpm, 1 min) from 1.25 mg/mL NP dispersions onto glass and coated with Pt (3 nm) to ensure sample conductivity. TEM images of the NPs were recorded using a JEOL 1200EX TEM operating at an accelerating voltage of 80 kV. The NP dispersions were spin-coated (3000 rpm, 1 min) onto silicon nitride window substrates with a silicon dioxide coating (250 μm × 250 μm window of 15 nm thickness) and air dried.

For UV–Vis and PL characterization, the relevant films were spin-coated onto quartz glass slides or measured as dispersions in quartz cuvettes. A UV–Vis absorption spectrophotometer (Varian Cary 6000i) was used to study the absorption of the nanoparticulate dispersions and films. PL measurements were conducted using a Cary Eclipse fluorescence spectrophotometer with an excitation wavelength of 410 nm. AFM was performed on a Cypher (Asylum Research) operating in alternating-current (AC) mode. Dispersion samples were prepared as for UV–Vis characterization. Film samples were prepared by spin-coating 70 mL P3HT:$PC_{61}BM$ 1:1 NPs onto a precleaned glass silica slide (2 cm × 2 cm), which was then dried on a hot plate at 110°C for 4 min.

Grazing-incidence x-ray diffraction analysis was performed using a Phillips X'PertPRO MPD XRD, equipped with a Co K_α anode (λ = 1.78901 Å). The angle of incidence was fixed at ω = 0.8°, and data were collected for ~ 1 h in the 2θ range from 3° to 35° in steps of 0.05°.

Device Fabrication

Standard sodium dodecyl sulfate (SDS)-stabilized NP-OPV devices were prepared as previously reported.[6] Patterned indium tin oxide (ITO) substrates were sourced from Xinyan Technology Ltd. with sheet resistance of 15 Ω/□ and optical transmission greater than 80%. The prepatterned ITO slides were cleaned in an ultrasonic bath using detergent, acetone, and isopropanol. After drying

the slides, 75 μl poly(3,4-ethylenedioxythiophene)/poly(styrenesulfonate) (PEDOT:PSS; Baytron P) solution was spin-coated onto each ITO slide at 4000 rpm for 60 s with acceleration of 1680 rpm/s to give an $\sim$ 50-nm-thick film. Immediately prior to deposition, the PEDOT:PSS solution was filtered through a 0.45-μm PVDF syringe filter to remove any large aggregates. The PEDOT:PSS-coated substrates were then placed on a hotplate and dried at 140°C for 30 min. For the active layers used in this study, the P3HT:$PC_{61}BM$ nanoparticle dispersion was deposited by pipetting 100 μL of solution onto each PEDOT:PSS-covered substrate, then spreading it evenly across the surface using the pipette tip. The substrate was then spun at 1000 rpm for 1 min with acceleration of 1600 rpm/s. The film was then dried between each layer deposition at 100°C for 3 min. Repeat dispersion depositions were undertaken until the desired numbers of layers and layer thickness were achieved. Once the final layer (1 to 10 layers) had been deposited, the substrate was annealed at 140°C for 4 min. Evaporative deposition of a final $\sim$ 100-nm-thick aluminum cathode at a rate of 2 Å/s was undertaken at a pressure below 2.7×10^{-7} kPa using an Ångstrom Engineering evaporator.

Device Characterization

Current–voltage (*I–V*) measurements were conducted using a Newport Class A solar simulator with an AM 1.5 spectral filter to illuminate the full cells. The light intensity was measured to be 100 mW/cm^2 by using a silicon reference solar cell (FHG-ISE), and the current–voltage (*I–V*) data were recorded using a Keithley 2400 source meter. All presented device characteristics were obtained from masked cells and recorded either "as spun" or following a postcathode deposition annealing treatment of 4 min at 140°C under dry N_2. EQE spectra were recorded using a lock-in amplifier to measure the photocurrent from the devices when illuminated by chopped light from an Osram 12-V 100-W HLX64625 tungsten halogen lamp passed through an Oriel Cornerstone 130 monochromator.

RESULTS AND DISCUSSION

Stable precipitated nanoparticle inks were prepared by optimizing the ink as a function of the nanoparticulate weight loading in the ethanol matrix. P3HT (2.5 mg) and $PC_{61}BM$ (2.5 mg) were dissolved in 670 μL $CHCl_3$, and this solution was then added by syringe to ethanol (at a ratio of 1 mL to 10 mL) to produce nanoparticle suspensions with weight loading ranging from 5 mg/mL to 0.5 mg/mL. Figure 1 shows these suspensions: (a) immediately after preparation, (b) 15 min after preparation, (c) 2 h after preparation, and (d) 2 days after preparation. It is clear from these images that the optimal weight loading of these materials was 1.25 mg/mL, above which immediate complete aggregation and precipitation of the nanoparticles occurred but below which slow aggregation occurred, while a low weight loading of the active materials led to poor-quality films after only 15 min of storage. By contrast, the 1.25 mg/mL suspension was stable for more than 4 days under ambient conditions; consequently, all subsequent experiments were conducted at this loading.

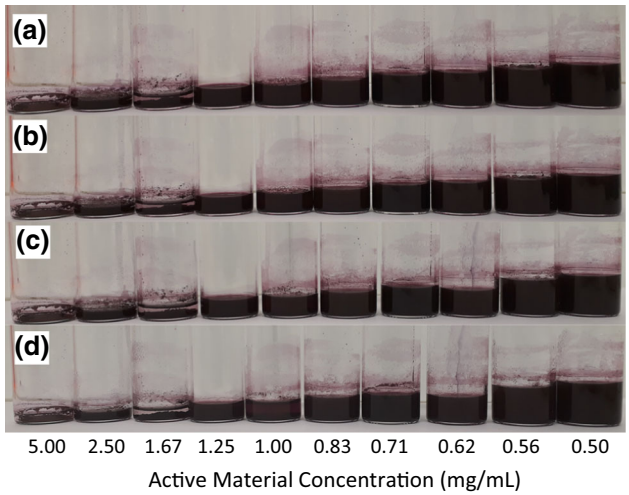

Fig. 1. P3HT:$PC_{61}BM$ (2.5 mg:2.5 mg) nanoparticle suspensions in ethanol (1 mL to 10 mL in 1-mL steps from left to right): (a) immediately after preparation, (b) 15 min after preparation, (c) 2 h after preparation, and (d) 2 days after preparation.

Figure 2a shows a TEM image of nanoparticles prepared as a 1.25 mg/mL suspension for film and device fabrication using the precipitation method. The TEM image shows the presence of discrete particles and confirms the DLS measurements for these dispersions which indicated a *z*-average diameter of 116 nm (Fig. 2b). The nanoparticle size can readily be scaled by altering the concentration of the P3HT:$PC_{61}BM$ solutions used in the nanoparticle fabrication, and the sizes utilized in this study were chosen as they have proven optimal for OPV device fabrication using this method.[15]

Figure 3 shows the UV–Vis spectra of the nanoparticle dispersion and films deposited on quartz slides, as a function of the number of deposition steps. The inset shows the absorbance of the as-spun and annealed films at 513 nm (the maximum absorbance for the P3HT component of the nanoparticles) as a function of the number of depositions. Trend lines, with R^2 values of 0.99 in both cases, have been added to highlight the systematic nature of these data. The UV–Vis absorbance increased linearly with the number of layers deposited, indicating that each subsequent deposition added the same mass of nanoparticles to the preexisting film without damaging or removing previously deposited NPs. Similar linear trends have been observed for systematic stepwise deposition of surfactant-stabilized NPs to prepare NP films.[19,20] The peak shape for the films shows vibronic peaks at $\sim$ 560 m, and 610 nm, which are

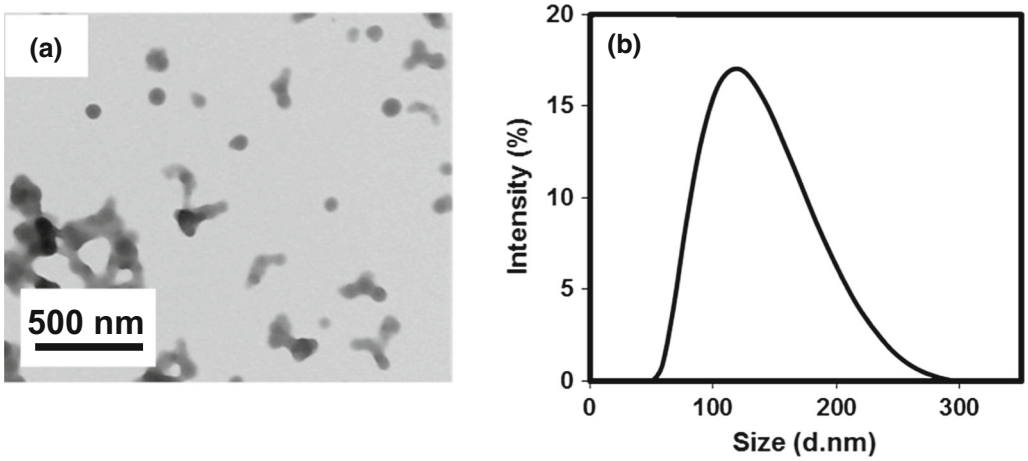

Fig. 2. (a) TEM image of as-cast surfactant-free P3HT:$PC_{61}BM$ nanoparticles. (b) DLS of as-fabricated surfactant-free NP dispersions.

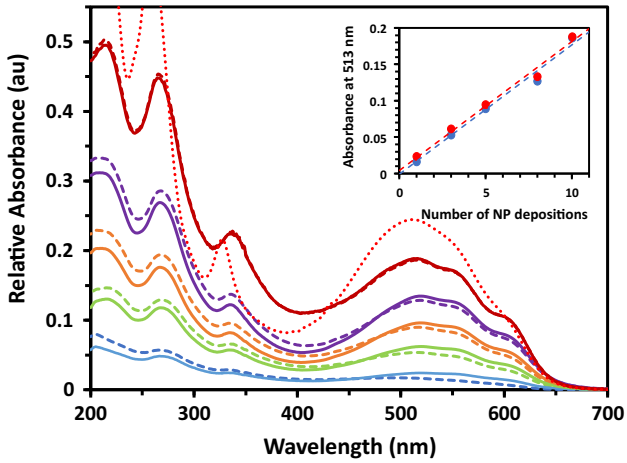

Fig. 3. UV–Vis relative absorbance as function of wavelength for films formed by one (light blue), three (light green), five (orange), eight (purple), and ten depositions (maroon), and ethanolic dispersion (red dots) of surfactant-free P3HT:$PC_{61}BM$ nanoparticles. Unannealed and annealed films are denoted by dashed and solid lines, respectively. The inset shows the relative absorbance at 513 nm as a function of nanoparticle depositions for unannealed (blue) and annealed (red) films; trend lines (R^2 = 0.99 for both datasets) are included to show the systematic nature of these data (Color figure online).

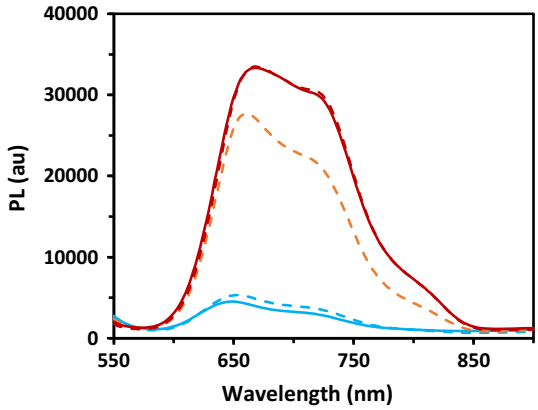

Fig. 4. Photoluminescence as function of wavelength for films formed from one (light blue), five (orange), and ten depositions (maroon) of surfactant-free P3HT:$PC_{61}BM$ nanoparticles. Unannealed and annealed films are denoted by dashed and solid lines, respectively (Color figure online).

typical of the formation of crystalline domains of P3HT during the nanoparticle formation process (although notably less crystalline than NPs prepared via the miniemulsion process with SDS surfactant[21]), and the overall spectral shape remained consistent throughout the series. These results confirm that neither the composition nor the relative crystallinity of the film was affected by the deposition steps or annealing.

Figure 4 shows the PL spectra for the unannealed films formed by one, five, and ten depositions of precipitated NPs and the annealed films formed by one and ten depositions. These spectra reveal that, as the number of depositions was increased, so did the total photoluminescence of the film. Interestingly, these data also show that thermal annealing of the films formed by one and ten depositions resulted in no change to the photoluminescence of the film. Thermal annealing is known to lead to a significant increase in the PL of P3HT:$PC_{61}BM$ BHJ films due to phase segregation of the P3HT and $PC_{61}BM$ into more pure phases and increased ordering of the P3HT polymer chains.[22] This result implies that heating the precipitated P3HT:$PC_{61}BM$ NPs did not lead to the expected phase segregation of the components or crystallization of the P3HT, but rather did not change the morphology of the NPs.

Nanoparticulate OPV devices were fabricated with active layers prepared by one, three, five, eight, and ten NP depositions. The devices were initially tested unannealed and after 4 min of thermal annealing treatment at 140°C. The best device parameters are presented in Table I and Fig. 5, and the current density–voltage (J–V) curves for these devices are shown in Fig. 6.

Single-deposition devices did not function as OPVs, exhibiting linear J–V plots which passed

Table I. Comparison of active layer thickness (the error is the standard deviation of three device measurements) and optimum device characteristics of NP-OPV devices fabricated for each number of dispersion depositions with surfactant-free P3HT:$PC_{61}BM$ 1:1 blend NPs

		J_{sc} (mA/cm^2)	V_{oc} (mV)	Fill Factor (FF)	η (%)	Thickness (nm)
One deposition	Unannealed	–	–	–	–	13 ± 2
	Annealed					
Three depositions	Unannealed	0.218	445	0.150	0.014	74 ± 1
	Annealed	0.659	375	0.206	0.051	
Five depositions	Unannealed	3.507	202	0.297	0.210	95 ± 1
	Annealed	4.235	364	0.324	0.499	
Eight depositions	Unannealed	1.294	480	0.287	0.178	152 ± 4
	Annealed	3.466	584	0.357	0.723	
Ten depositions	Unannealed	0.345	236	0.196	0.160	205 ± 3
	Annealed	7.144	538	0.192	0.738	

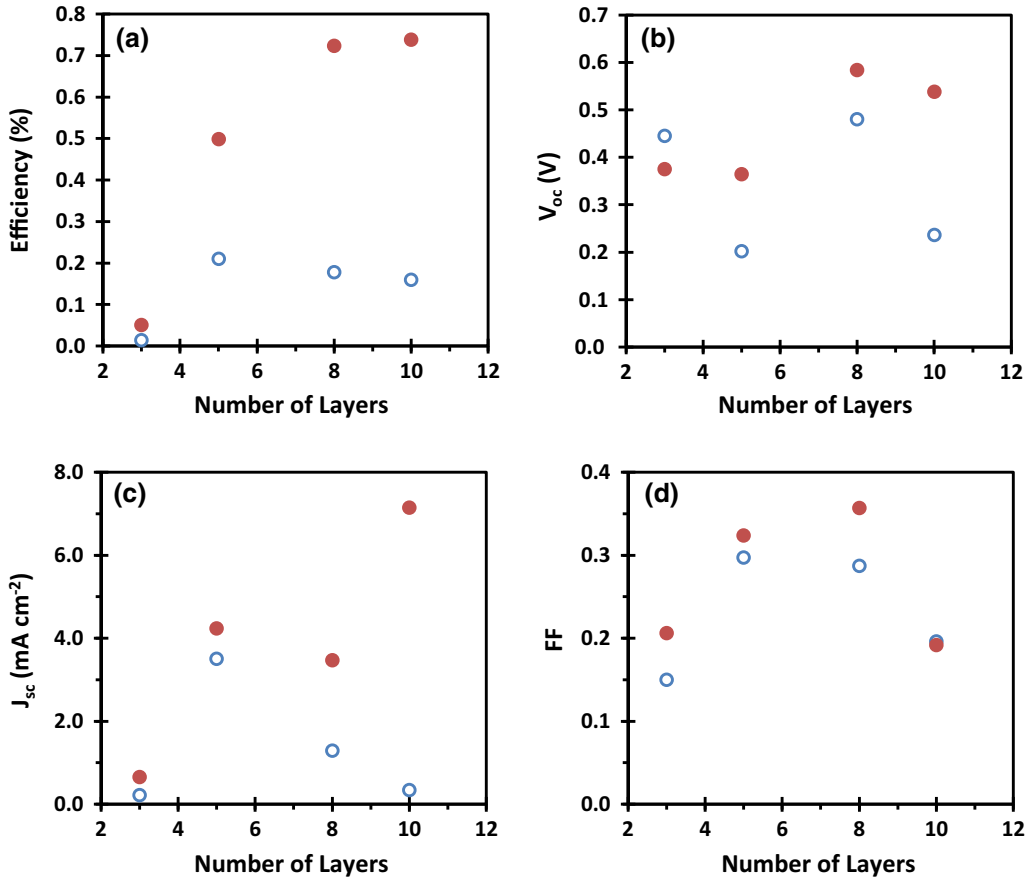

Fig. 5. Best (a) efficiency, (b) V_{oc}, (c) J_{sc}, and (d) FF for non-SDS-stabilized P3HT:$PC_{61}BM$ nanoparticle devices as functions of number of NP depositions. Blue circles indicate unannealed devices; red dots indicate devices annealed for 4 min at 140°C (Color figure online).

through the origin, typical of electrically short-circuited devices. All of the unannealed devices showed poor efficiencies (< 0.2%), with no obvious systematic trends in the device parameters, although interestingly the devices obtained by five depositions consistently showed the highest short-circuit current density (J_{sc}) but lowest open-circuit voltage (V_{oc}). By contrast, the annealed (4 min at 140°C) devices showed a systematic increase in efficiency with the number of NP depositions, even though the device parameters did not display the same systematic trend. Indeed, the J–V curves transitioned from "S" shape (three layers) to "J" shape (five and eight layers) then back to "S" shape (ten layers), indicating a dramatic change in the degree of charge recombination in these devices. Table I also presents the average film thickness for the active layers as a function of the number of NP

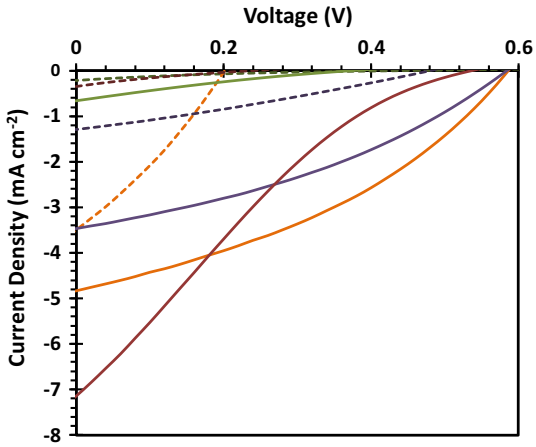

Fig. 6. Current density–voltage graphs for best non-SDS-stabilized P3HT:$PC_{61}BM$ nanoparticle devices as function of number of NP depositions: three (light green), five (orange), eight (purple), and ten (maroon) of surfactant-free P3HT:$PC_{61}BM$ nanoparticles. Unannealed and annealed (4 min at 140 ºC) films are denoted by dashed and solid lines, respectively (Color figure online).

deposition steps. These data are consistent with the UV–Vis data presented in Fig. 3 and reveal that the layer thickness increased linearly (R^2 = 0.99) with the number of NP depositions. Again, a similar linear increase in film thickness was observed during the systematic deposition of the individual layers of surfactant-stabilized NPs onto a NP film. However, in the case of the precipitated NPs, the average film thickness increased by only ~ 20 nm per NP deposition, implying that each additional deposition served to fill defects in the film topography rather than add a new complete NP layer (since the *z*-average diameter of the NPs is 116 nm). The fact that the particle size distribution was broad (ranging from < 50 nm to > 300 nm) assisted with this film infilling process.

Figure 7 shows AFM images of the as-cast and annealed films obtained by one, three, five, eight, and ten depositions. The images show that the films were rough and composed of distinct NPs, but that they were also incomplete below five depositions, with dark voids and patches of bare substrate present in each film. Annealing smoothed the films and led to some joining of the NPs. Table II presents the maximum NP film height and root-mean-square (RMS) roughness obtained from each AFM image in Fig. 7a–j. The tabulated data show that the film height and roughness did not change significantly with increasing number of depositions or annealing of the films, suggesting that the sequential depositions were even across the substrate surface.

This phenomenon is more clearly seen in Fig. 8, which depicts SEM images of the as-cast and annealed films obtained by one, three, five, and eight depositions. In these images, the incomplete nature of the films obtained by one, three, and five depositions is evident, with complete film formation only observed for the annealed film after five depositions and as-cast and annealed films after eight depositions. These images provide an explanation for the observed performance of the respective OPV devices. The as-cast films obtained by one, three, and five depositions are incomplete and patchy and, as such, the performance of the corresponding devices is poor at best. The film obtained by five deposition is the first complete layer, and this film becomes smoother and more uniform after annealing. Beyond five depositions, the films appear to become patchier again, with large aggregates and steps (of hundreds of nanometers in scale) being observed. Despite this change, the devices using the as-cast films obtained by eight and ten depositions performed better than the equivalent device obtained using five depositions due to the improved film connectivity. Annealing these films improved the topography, but not to the degree observed in the case of five depositions, thus the relative device performance was still lower.

These results enable an interesting comparison of the performance of the precipitated NP-OPV devices with previously reported SDS-surfactant-stabilized NP-OPV devices. The optimal SDS-stabilized NP devices were composed of NPs with *z*-average diameter of 31.5 nm, much smaller than the 116-nm NPs used in this precipitated NP study. This smaller optimal size is a direct requirement of the $PC_{61}BM$-rich core, P3HT-rich shell, core–shell morphology of the SDS-stabilized NPs, a morphology which has been suggested to limit charge generation and transport within these devices.[14] By comparison, the precipitated NPs had a much more blended morphology, resembling that of a P3HT:$PC_{61}BM$ BHJ OPV device, and the resulting device performance was much less dependent on the active material domain sizes, which are dictated by the surfactant-stabilized NP morphology and size.

To fully explore the effect of thermal annealing on the morphology of the active layer film and the device performance, extended annealing was conducted on the precipitated NP-OPV devices. For this study, standard SDS-stabilized NP-OPV devices were also prepared, as previously reported,[6] and annealed for further comparison with the precipitated NP-OPV devices. Table III presents the device parameters for the average precipitated and SDS-stabilized NP-OPV devices, while Fig. 9 compares the *J*–*V* curves, EQE spectra, and UV–Vis spectra of the precipitated and SDS-stabilized NP-OPV devices with five layers.

Interestingly, both the SDS-stabilized and precipitated NP-OPV devices performed optimally when five deposition steps were applied. In the case of the SDS-stabilized films, five deposition steps resulted in the addition of five full NP monolayers and an overall film thickness of ~ 190 nm. The optimal device performance was reached after a short (4 min) annealing step. By comparison, five depositions of precipitated NPs were required to merely complete a NP layer, resulting in a film of only approximately one half the thickness. In this case,

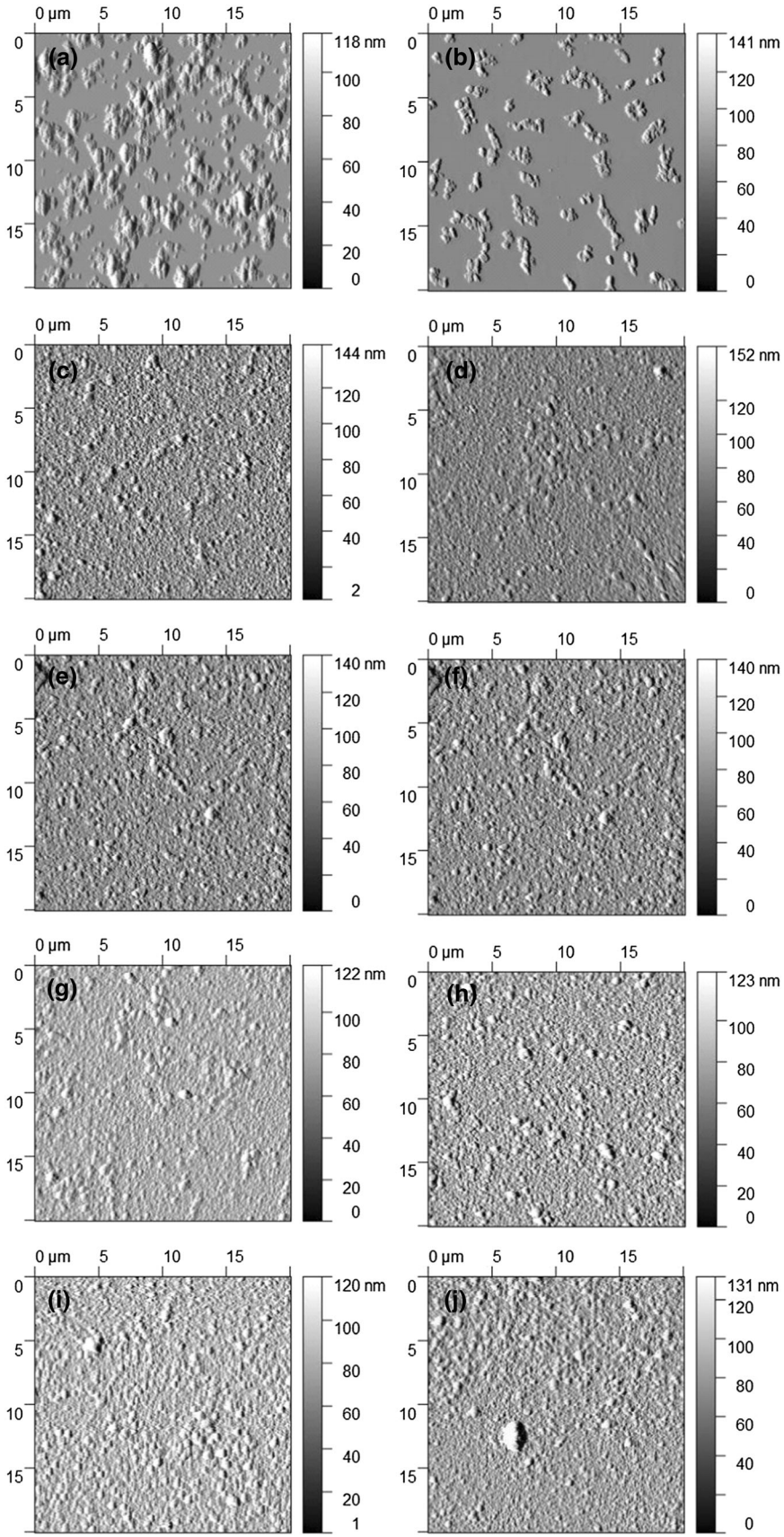

Fig. 7. AFM images (20 μm $\times$ 20 μm) of surfactant-free P3HT:PC_{61}BM nanoparticle films obtained by one (a, b), three (c, d), five (e, f), eight (g, h), and ten depositions (i, j) for as-spun nanoparticles (a, c, e, g, i) and after annealing for 4 min at 140°C (b, d, f, h, j).

Table II. Maximum film height and RMS roughness obtained from AFM images in Fig. 7

		Unannealed		Annealed (4 min at 140°C)	
		Maximum Height (nm)	RMS Roughness (nm)	Maximum Height (nm)	RMS Roughness (nm)
One deposition	Fig. 7a, b	118	19	141	17
Three depositions	Fig. 7c, d	144	27	152	22
Five depositions	Fig. 7e, f	140	25	140	26
Eight depositions	Fig. 7g, h	122	18	123	25
Ten depositions	Fig. 7i, j	120	23	131	25

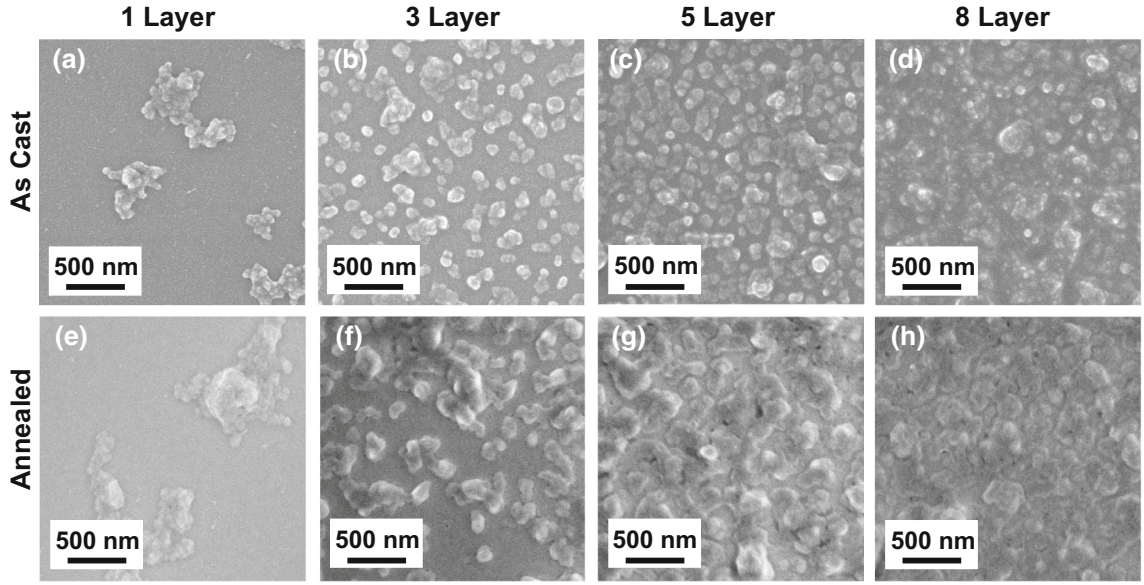

Fig. 8. SEM images of precipitated P3HT:$PC_{61}BM$ NP films as a function of deposition number: (a, e) one, (b, f) three, (c, g) five, and (d, h) eight, in as-cast state (a–d) and after 4 min of annealing at 140°C (e–h).

extended annealing (over 1 h) led to the optimal device performance.

The UV–Vis spectra of the active layers of these two devices (Fig. 9b) were consistent with these thickness measurements and showed that the SDS-stabilized active layer contained more than twice as much P3HT and $PC_{61}BM$ as the precipitated NP film. Despite this difference, as has been observed previously, the precipitated devices outperformed their SDS counterparts by more than a factor of two, due to increases in their J_{sc} and V_{oc}. The EQE plots in Fig. 9c confirmed the enhanced photocurrent of the precipitated device. Using a combination of modeling and experimental techniques, Al-Mudhaffer et al. determined that the poor photocurrent of SDS-stabilized NP-OPVs was a consequence of a poor charge generation yield.[14] These results show that this low photocurrent is not inherent to a NP active layer but must result from the nonoptimal core–shell morphology of the surfactant-stabilized NPs.

Clearly, a key difference between the precipitated and SDS-stabilized NP-OPV devices lies in their response to extended thermal annealing. Figure 10 shows how the device efficiency changed as a function of the annealing time (at 140°C) for the NP-OPV devices with precipitated and SDS-stabilized NP active layers. Initially, both sets of devices showed very similar device performance. However, the performance of the precipitated NP-OPV devices increased systematically with the annealing time, until stable performance was reached after $\sim$ 30 min. This increase was a result of increases in both J_{sc} and V_{oc}, and beyond the half-hour mark, further heating led to no further changes in the average device performance. This improvement was even more marked for the optimized devices, which systematically improved for up to an additional 1 h

Table III. Comparison of device parameters for average five-deposition precipitated and five-layer SDS-stabilized NP-OPV devices from Ref. 20 and standardized SDS-stabilized NP-OPV devices

	J_{sc} (mA/cm^2)	V_{oc} (mV)	FF	η (%)
Five-layer SDS-stabilized NP-OPV				
Unannealed	2.18 ± 0.30	332 ± 94	0.28 ± 0.01	0.20 ± 0.07
4 min at 140°C	3.62 ± 0.27	419 ± 12	0.34 ± 0.01	0.52 ± 0.27
Standard SDS-stabilized NP-OPV				
Unannealed	2.23 (2.55)	360 (450)	0.41 (0.43)	0.33 (0.49)
3 min at 140°C	2.14 (2.83)	400 (480)	0.39 (0.38)	0.33 (0.52)
4 min at 140°C	2.61 (2.99)	430 (450)	0.43 (0.41)	0.48 (0.55)
5 min at 140°C	2.93 (3.17)	410 (430)	0.41 (0.42)	0.49 (0.57)
10 min at 140°C	2.26 (3.03)	340 (390)	0.33 (0.38)	0.25 (0.45)
15 min at 140°C	2.17 (2.76)	350 (380)	0.34 (0.39)	0.26 (0.41)
30 min at 140°C	1.99 (2.10)	280 (330)	0.34 (0.39)	0.19 (0.27)
60 min at 140°C	–	–	–	–
Five-deposition precipitated NP-OPV				
Unannealed	2.95 ± 0.30 (3.51)	162 ± 37 (202)	0.29 ± 0.01 (0.30)	0.14 ± 0.08 (0.21)
4 min at 140°C	3.82 ± 0.42 (4.23)	347 ± 87 (364)	0.32 ± 0.02 (0.32)	0.42 ± 0.17 (0.50)
19 min at 140°C	3.82 ± 0.44 (4.50)	347 ± 57 (428)	0.32 ± 0.01 (0.33)	0.42 ± 0.13 (0.64)
34 min at 140°C	4.12 ± 0.41 (4.60)	448 ± 90 (450)	0.34 ± 0.02 (0.33)	0.63 ± 0.20 (0.69)
49 min at 140°C	4.15 ± 0.40 (4.59)	461 ± 87 (464)	0.34 ± 0.02 (0.33)	0.65 ± 0.20 (0.70)
64 min at 140°C	4.16 ± 0.37 (4.83)	458 ± 95 (559)	0.34 ± 0.02 (0.36)	0.65 ± 0.21 (0.95)

Optimized device performance shown in parentheses.

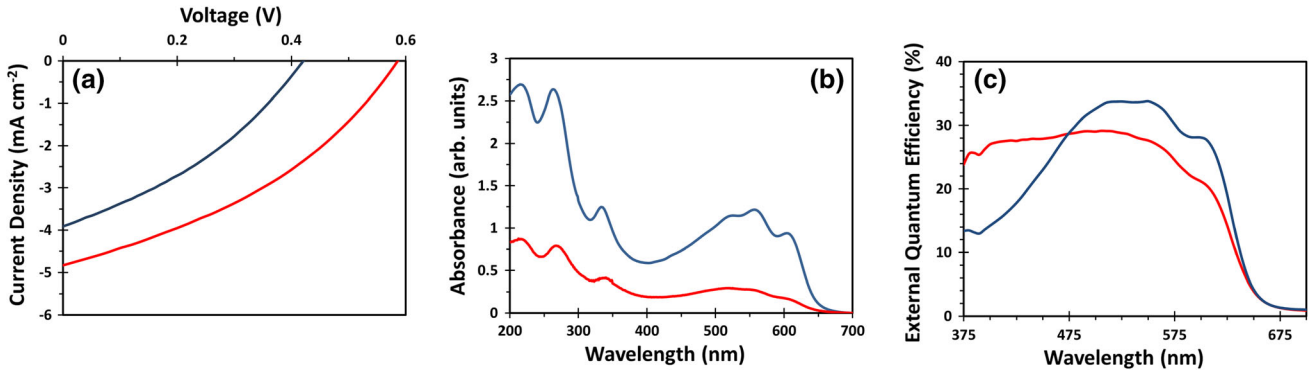

Fig. 9. Comparison of *J–V* curves (a), UV–Vis spectra (b), and EQE spectra (c) for optimized five-deposition precipitated NP-OPV device (red lines) and optimized five-layer SDS-stabilized NP-OPV device from Ref. 20 (blue lines) (Color figure online).

of annealing time (at which point the device performance began to drop again). By contrast, extended annealing of the devices obtained by eight or ten depositions did not result in significant changes to the device performance. By comparison, the performance of the surfactant-stabilized NP-OPV devices reached a maximum after only 4 min of annealing at 140°C; then, with continued heating, the device performance dropped rapidly until the devices no longer functioned after 60 min of heating.

The observed thermal trends are readily explained by, and provide insight into, the morphological changes that occur in the NP active layers upon thermal treatment. Thermally driven morphological changes are a significant challenge in OPV development, with it being well known that BHJ P3HT:$PC_{61}BM$ devices undergo extensive phase segregation upon even moderate thermal annealing. Berriman et al. showed that small (20 nm) $PC_{61}BM$ crystallites initially formed in the P3HT matrix during the BHJ film formation process.[23–25] $PC_{61}BM$ crystallites below this size threshold are thermodynamically unstable and will redissolve into the P3HT matrix. Upon heating, molecular growth of these crystallites occurs until crystallites of ~ 50 nm are formed and a stable neighboring blend composition of 20% $PC_{61}BM$ is reached. Continued heating results in slow aggregation of these $PC_{61}BM$ crystallites, and micron-scale phase segregation occurs after extended annealing times in Fig. 11a.

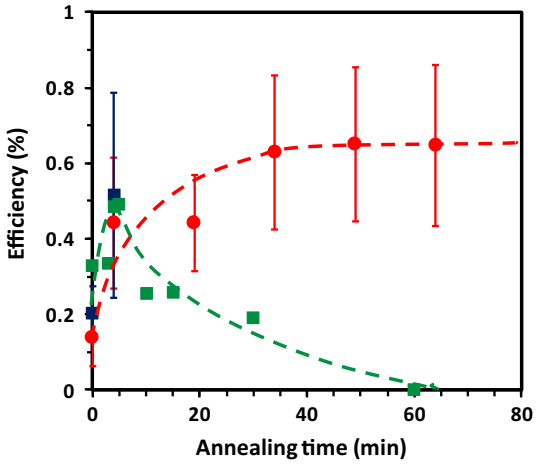

Fig. 10. Device efficiency as function of annealing time (at 140°C) for the average five-deposition precipitated NP-OPV devices (red circles), average five-layer SDS-stabilized NP-OPV devices (blue squares) in Ref. 20, and average standard SDS-stabilized P3HT:$PC_{61}BM$ NP-OPV devices (green squares). Dashed red and green trend lines have been superimposed on the data as guides to the eye (Color figure online).

The miniemulsion process results in surfactant-stabilized NPs which have a core–shell morphology, with a $PC_{61}BM$-rich core which is very similar in size, composition, and crystallinity to the $PC_{61}BM$ crystallites initially observed in BHJ films. Molecular core growth can occur within the NPs during annealing, and upon extended annealing core migration is observed, resulting in a P3HT-rich residual shell phase and $PC_{61}BM$ aggregates in Fig. 11b.[26] Thus, for both BHJ and surfactant-stabilized NP P3HT:$PC_{61}BM$ films, extended annealing results in gross phase segregation and degradation of OPV functionality.

By contrast, the precipitation method for producing P3HT:$PC_{61}BM$ NPs appears to result in a more molecularly blended morphology. The fact that the UV–Vis spectra show evidence of vibronic peaks in Fig. 3 and the PL spectra do show significant emission from P3HT in Fig. 4 implies that crystalline P3HT domains do exist in the precipitated NP films. Figure 12 shows the grazing-incidence x-ray diffractogram (GIXRD) analysis of an annealed BHJ P3HT:$PC_{61}BM$ and films of precipitated P3HT:$PC_{61}BM$ NPs in the as-spun state and after annealing for 4 min and 60 min. The BHJ diffractogram shows the expected features indicating the presence of crystalline P3HT domains; a (100) reflection peak due to the lamellar layered structure (at $\sim 5.4°$), with (200) ($\sim 10.6°$) and (300) ($\sim 20.9°$) diffraction peaks indicating crystallinity with edge-on chain orientation and an out-of-plane reflection peak (010) due to π–π interchain stacking ($\sim 23.4°$).[27] In addition, a broad peak is observed at $\sim 19.5°$, corresponding to a small contribution from $PC_{61}BM$ crystallites.[28] Analysis of the $PC_{61}BM$ peak using the Scherrer equation yields a mean size for these crystallites of approximately 21 nm, in good agreement with a previous report.[25] By contrast, the diffractogram of the as-spun precipitated NP film showed little evidence of P3HT crystallinity, and no $PC_{61}BM$ crystallinity, indicating that the precipitated particles were initially highly molecularly blended. After 4 min of annealing, evidence of P3HT crystallization was observed. After 60 min of annealing, the intensity of the P3HT crystalline peaks increased and a small peak corresponding to $PC_{61}BM$ crystallites appeared. This $PC_{61}BM$ peak was much sharper than that observed for the BHJ film, and application of the Scherrer equation showed that these crystallites had a mean size of 57 nm, in good agreement with the size of $PC_{61}BM$ crystallites present in the $PC_{61}BM$ aggregates observed by Berriman et al. upon annealing of P3HT:$PC_{61}BM$ films.[25]

As such, annealing of the initially blended precipitated NP films resulted in two phases: one crystalline P3HT, and the second composed of molecularly mixed P3HT:$PC_{61}BM$. The rapid precipitation of the active materials means that thermodynamically stable $PC_{61}BM$ crystallites are not formed during the precipitated NP synthesis, thus there is no drive for phase segregation to occur upon thermal annealing. Consequently, it is only after extended annealing that $PC_{61}BM$ crystallites start to form via molecular growth, and extended thermal annealing of precipitated NP films does not lead to gross phase segregation but serves only to improve the film morphology through sintering of the particles and smoothing of the film in Fig. 11c. As a result, the device performance improves with thermal annealing until a stable optimal morphology is reached, and gross phase segregation does not occur thermally.

This result has significant consequences for OPV development. The loss of device performance due to thermal annealing and phase segregation at OPV operating temperatures ($\sim 80°C$) is currently a significant hurdle to the viability of organic solar modules. The long-term thermal stability and ability to thermally condition the morphology of precipitated NP-OPV devices offers a clear pathway to improving the efficiency of NP-OPV devices as well as the stability and lifetime of OPV modules in general.

CONCLUSIONS

Stable aqueous P3HT:$PC_{61}BM$ NP inks were prepared by the precipitation method and used to prepare NP-OPV devices. An optimal P3HT:$PC_{61}BM$ weight loading and extended annealing resulted in highly stable NP inks that produced NP-OPV devices that generated more photocurrent and were twice as efficient as equivalent surfactant-stabilized NP-OPV devices. Structural and morphological studies using AFM, SEM, and GIXRD analysis revealed that the precipitated NP films exhibited excellent thermal stability. In

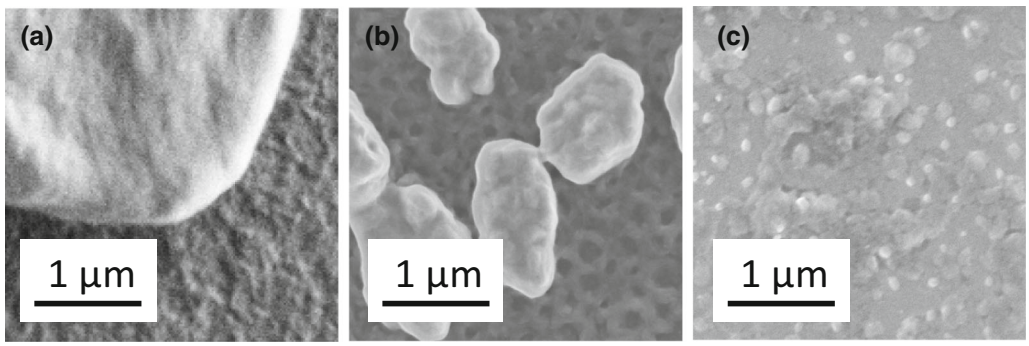

Fig. 11. SEM images (2.5 μm $\times$ 2.5 μm) of P3HT:PC_{61}BM BHJ film (annealed at 150°C for 20 min) (a), P3HT:PC_{61}BM SDS-stabilized NP film (annealed at 140°C for 10 min) (b), and P3HT:PC_{61}BM precipitated NP film (annealed at 140°C for 60 min) (c).

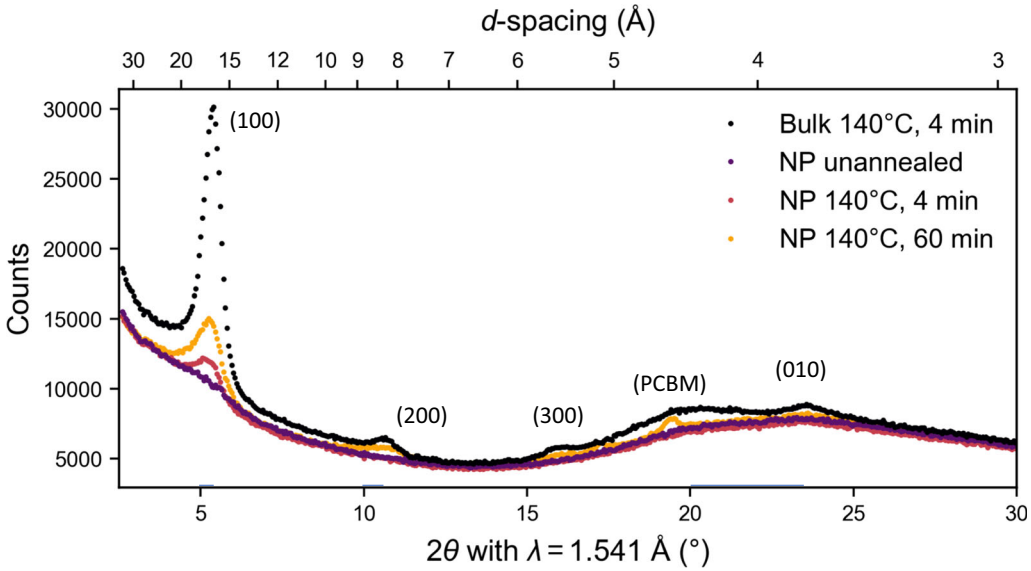

Fig. 12. Grazing-incidence x-ray diffractograms of P3HT:PC_{61}BM BHJ film (annealed at 140°C for 4 min) and P3HT:PC_{61}BM precipitated NP films (as spun and annealed at 140°C for 4 min and 60 min).

particular, whereas BHJ and surfactant-stabilized NP active layers undergo gross phase segregation upon extended thermal annealing, crystallization of the PC_{61}BM component was not observed under moderate annealing of the precipitated NPs. Instead, annealing served only to join and smooth the active layer, improving the device performance. Consequently. the molecularly blended morphology observed in precipitated NPs may serve as a pathway to NP-OPV devices with both high thermal stability and efficiencies approaching those of BHJ OPV devices.

ACKNOWLEDGMENTS

This research was supported by the Priority Research Centre for Organic Electronics, University of Newcastle. The work was also performed in part at the Materials Node of the Australian National Fabrication Facility, which is a company established under the National Collaborative Research Infrastructure Strategy to provide nano- and microfabrication facilities for Australia's researchers. P.C.D., D.D., and E.S. gratefully acknowledge support from the Indonesian Directorate for Higher Education (DIKTI) program funding.

REFERENCES

1. R.R. Søndergaard, M. Hösel, and F.C. Krebs, *J. Polym. Sci. B* 51, 16 (2013).
2. C. McDowell, and G.C. Bazan, *Curr. Opin. Green Sustain. Chem.* 5, 4 (2017).
3. L. D'Olieslaeger, M. Pfannmöller, E. Fron, I. Cardinaletti, M. Van Der Auweraer, G. Van Tendeloo, S. Bals, W. Maes, D. Vanderzande, J. Manca, and A. Ethirajan, *Sol. Energy Mater. Sol. Cells* 159, 179 (2017).
4. N.P. Holmes, M. Marks, J.M. Cave, K. Feron, M.G. Barr, A. Fahy, A. Sharma, X. Pan, D.A.L. Kilcoyne, X. Zhou, D.A. Lewis, M.R. Andersson, J. van Stam, A.B. Walker, E. Moons, W.J. Belcher, and P.C. Dastoor, *Chem. Mater.* 30, 6521 (2018).
5. N.P. Holmes, M. Marks, P. Kumar, R. Kroon, M.G. Barr, N. Nicolaidis, K. Feron, A. Pivrikas, A. Fahy, A.D.D.Z. Mendaza, A.L.D. Kilcoyne, C. Müller, X. Zhou, M.R. Andersson, P.C. Dastoor, and W.J. Belcher, *Nano Energy* 19, 495 (2016).

6. S. Ulum, N. Holmes, M. Barr, A.L.D. Kilcoyne, B. Bin Gong, X. Zhou, W. Belcher, and P. Dastoor, *Nano Energy* 2, 897 (2013).
7. X. Pan, A. Sharma, D. Gedefaw, R. Kroon, A. Diaz Zerio, N.P. Holmes, A.L.D. Kilcoyne, M.G. Barr, A. Fahy, M. Marks, X. Zhou, W. Belcher, P.C. Dastoor, and M.R. Andersson, *Org. Electron. Phys. Mater. Appl.* 59, 432 (2018).
8. M. Marks, N.P. Holmes, A. Sharma, X. Pan, R. Chowdhury, M.G. Barr, C. Fenn, M.J. Griffith, K. Feron, A.L.D. Kilcoyne, D.A. Lewis, M.R. Andersson, W.J. Belcher, and P.C. Dastoor, *Phys. Chem. Chem. Phys.* 21, 5705 (2019).
9. F.J.M. Colberts, M.M. Wienk, and R.A.J. Janssen, *ACS Appl. Mater. Interfaces* 9, 13380 (2017).
10. C. Xie, A. Classen, A. Späth, X. Tang, J. Min, M. Meyer, C. Zhang, N. Li, A. Osvet, R.H. Fink, and C.J. Brabec, *Adv. Energy Mater.* 8, 1702857 (2018).
11. M. Bag, T.S. Gehan, D.D. Algaier, F. Liu, G. Nagarjuna, P.M. Lahti, T.P. Russell, and D. Venkataraman, *Adv. Mater.* 25, 6411 (2013).
12. M. Ameri, M.F. Al-Mudhaffer, F. Almyahi, G.C. Fardell, M. Marks, A. Al-Ahmad, A. Fahy, T. Andersen, D.C. Elkington, K. Feron, M. Dickinson, F. Samavat, P.C. Dastoor, and M.J. Griffith, *ACS Appl. Mater. Interfaces* 11, 10074 (2019).
13. C. Xie, T. Heumüller, W. Gruber, X. Tang, A. Classen, I. Schuldes, M. Bidwell, A. Späth, R.H. Fink, T. Unruh, I. Mcculloch, N. Li, and C.J. Brabec, *Nat. Commun.* 9, 5335 (2018).
14. M.F. Al-Mudhaffer, M.J. Griffith, K. Feron, N.C. Nicolaidis, N.A. Cooling, X. Zhou, J. Holdsworth, W.J. Belcher, and P.C. Dastoor, *Sol. Energy Mater. Sol. Cells* 175, 77 (2018).
15. D. Darwis, N. Holmes, D. Elkington, A.L. David Kilcoyne, G. Bryant, X. Zhou, P. Dastoor, and W. Belcher, *Sol. Energy Mater. Sol. Cells* 121, 99 (2014).
16. C. Xie, X. Tang, M. Berlinghof, S. Langner, S. Chen, A. Späth, N. Li, R.H. Fink, T. Unruh, and C.J. Brabec, *ACS Appl. Mater. Interfaces* 10, 23225 (2018).
17. S. Gärtner, M. Christmann, S. Sankaran, H. Röhm, E.-M. Prinz, F. Penth, A. Pütz, A.E. Türeli, B. Penth, B. Baumstümmler, and A. Colsmann, *Adv. Mater.* 26, 6653 (2014).
18. S. Sankaran, K. Glaser, S. Gärtner, T. Rödlmeier, K. Sudau, G. Hernandez-Sosa, and A. Colsmann, *Org. Electron.* 28, 118 (2016).
19. A. Stapleton, B. Vaughan, B. Xue, E. Sesa, K. Burke, X. Zhou, G. Bryant, O. Werzer, A. Nelson, A.L. David Kilcoyne, L. Thomsen, E. Wanless, W. Belcher, and P. Dastoor, *Sol. Energy Mater. Sol. Cells* 102, 114 (2012).
20. B. Vaughan, A. Stapleton, E. Sesa, N.P. Holmes, X. Zhou, P.C. Dastoor, and W.J. Belcher, *Org. Electron.* 32, 250 (2016).
21. N.P. Holmes, S. Ulum, P. Sista, K.B. Burke, M.G. Wilson, M.C. Stefan, X. Zhou, P.C. Dastoor, and W.J. Belcher, *Sol. Energy Mater. Sol. Cells* 128, 369 (2014).
22. S.S. van Bavel, M. Bärenklau, G. de With, H. Hoppe, and J. Loos, *Adv. Funct. Mater.* 20, 1458 (2015).
23. G.A. Berriman, J.L. Holdsworth, X. Zhou, W.J. Belcher, and P.C. Dastoor, *AIP Adv.* 5, 97220 (2015).
24. G.A. Berriman, J.L. Holdsworth, X. Zhou, W.J. Belcher, and P.C. Dastoor, *Org. Electron.* 38, 15 (2016).
25. G.A. Berriman, N.P. Holmes, J.L. Holdsworth, X. Zhou, W.J. Belcher, and P.C. Dastoor, *Org. Electron.* 30, 12 (2016).
26. N.P. Holmes, K.B. Burke, P. Sista, M. Barr, H.D. Magurudeniya, M.C. Stefan, A.L.D. Kilcoyne, X. Zhou, P.C. Dastoor, and W.J. Belcher, *Sol. Energy Mater. Sol. Cells* 117, 437 (2013).
27. W. Wang, C. Chen, C. Tollan, F. Yang, Y. Qin, and M. Knez, *J. Mater. Chem. C* 5, 2686 (2017).
28. Y. Zhong, K. Suzuki, D. Inoue, D. Hashizume, S. Izawa, K. Hashimoto, T. Koganezawa, and K. Tajima, *J. Mater. Chem. C* 4, 3335 (2016).